



# Near L-edge Single and Multiple Photoionization of Doubly Charged Iron Ions

Stefan Schippers<sup>1</sup> , Randolph Beerwerth<sup>2,3</sup> , Sadia Bari<sup>4</sup> , Ticia Buhr<sup>1</sup> , Kristof Holste<sup>1</sup> , A. L. David Kilcoyne<sup>5</sup> , Alexander Perry-Sassmannshausen<sup>1</sup> , Ronald A. Phaneuf<sup>6</sup>, Simon Reinhardt<sup>7</sup>, Daniel Wolf Savin<sup>8</sup> , Kaja Schubert<sup>4</sup> ,  
Stephan Fritzsche<sup>2,3</sup> , Michael Martins<sup>7</sup> , and Alfred Müller<sup>9</sup>

<sup>1</sup> I. Physikalisches Institut, Justus-Liebig-Universität Gießen, Heinrich-Buff-Ring 16, 35392 Giessen, Germany; [stefan.schippers@physik.uni-giessen.de](mailto:stefan.schippers@physik.uni-giessen.de)

<sup>2</sup> Helmholtz-Institut Jena, Fröbelstieg 3, 07743 Jena, Germany

<sup>3</sup> Theoretisch-Physikalisches Institut, Friedrich-Schiller-Universität Jena, 07743 Jena, Germany

<sup>4</sup> Deutsches Elektronen-Synchrotron DESY, Notkestrae 85, 22607 Hamburg, Germany

<sup>5</sup> Advanced Light Source, MS 80RO114, Lawrence Berkeley National Laboratory, Berkeley, CA 94720, USA

<sup>6</sup> Department of Physics, University of Nevada, Reno, NV 89557-0220, USA

<sup>7</sup> Institut für Experimentalphysik, Universität Hamburg, Luruper Chaussee 149, 22761 Hamburg, Germany

<sup>8</sup> Columbia Astrophysics Laboratory, Columbia University, 550 West 120th Street, New York, New York 10027, USA

<sup>9</sup> Institut für Atom- und Molekülphysik, Justus-Liebig-Universität Gießen, Leihgesterner Weg 217, 35392 Giessen, Germany

Received 2020 October 1; revised 2020 November 17; accepted 2020 November 18; published 2021 February 11

## Abstract

Using the photon–ion merged-beams technique at a synchrotron light source, we have measured relative cross sections for single and up to five-fold photoionization of  $\text{Fe}^{2+}$  ions in the energy range of 690–920 eV. This range contains thresholds and resonances associated with ionization and excitation of  $2p$  and  $2s$  electrons. Calculations were performed to simulate the total absorption spectra. The theoretical results show very good agreement with the experimental data, if overall energy shifts of up to 2.5 eV are applied to the calculated resonance positions and assumptions are made about the initial experimental population of the various levels of the  $\text{Fe}^{2+}([\text{Ar}]3d^6)$  ground configuration. Furthermore, we performed extensive calculations of the Auger cascades that result when an electron is removed from the  $2p$  subshell of  $\text{Fe}^{2+}$ . These computations lead to a better agreement with the measured product-charge-state distributions as compared to earlier work. We conclude that the  $L$ -shell absorption features of low-charged iron ions are useful for identifying gas-phase iron in the interstellar medium and for discriminating against the various forms of condensed-phase iron bound to composite interstellar dust grains.

*Unified Astronomy Thesaurus concepts:* [Interstellar atomic gas \(833\)](#); [Interstellar clouds \(834\)](#); [Interstellar medium \(847\)](#); [Interstellar absorption \(831\)](#); [Line intensities \(2084\)](#); [Atomic spectroscopy \(2099\)](#); [Line positions \(2085\)](#); [X-ray astronomy \(1810\)](#); [Laboratory astrophysics \(2004\)](#)

*Supporting material:* machine-readable table

## 1. Introduction

$L$ -shell photoionization data of low-charged iron ions are required to reliably assess the abundance of iron in the interstellar medium (ISM) from astronomical X-ray observations. Resonant  $L$ -shell absorption features offer the possibility to discriminate between iron in the gas phase and iron that is chemically bound in dust grains. Absorption data for chemically bound iron are available from the literature (e.g., Kortricht & Kim 2000; Lee et al. 2009; Miedema & de Groot 2013; Westphal et al. 2019). However, corresponding experimental data for low-charged iron ions had been missing. In order to fill this gap we have launched a campaign to provide absorption data for  $\text{Fe}^+$ ,  $\text{Fe}^{2+}$ , and  $\text{Fe}^{3+}$  ions using photon–ion merged-beams measurements at a synchrotron light source and accompanying theoretical calculations. Results for  $\text{Fe}^+$  and  $\text{Fe}^{3+}$  ions have already been published by Schippers et al. (2017) and Beerwerth et al. (2019), respectively. The photoabsorption cross section of neutral  $\text{Fe}^0$  had already been measured previously by Richter et al. (2004). Experimental cross sections for  $L$ -shell photoionization of more highly charged iron ions are also available (Simon et al. 2010; Blancard et al. 2018), but these are unimportant for the determination of the abundance of iron in the cold ISM.

In this work, we present our measurements of relative cross sections for up to five-fold ionization of  $\text{Fe}^{2+}$  ions via ionization or excitation of the  $L$ -shell. These data provide, in particular, accurate information on the positions and shapes of photoionization

resonances associated with the excitation of a  $2p$  electron. The data will also facilitate a reliable identification of  $\text{Fe}^{2+}$  absorption features in, for example, astrophysical X-ray spectra. Furthermore, extensive quantum theoretical calculations to simulate the experimental spectra and to identify the dominant decay channels were performed. These results are vital for determining the charge balance and elemental abundance in astrophysical plasmas.

The  $\text{Fe}^+$  and  $\text{Fe}^{3+}$  papers (Schippers et al. 2017; Beerwerth et al. 2019) provide an extended motivation for these investigations and a comprehensive discussion of the related literature. Therefore, the present paper confines itself primarily to the aspects that are specific for  $L$ -shell photoionization and photoabsorption of  $\text{Fe}^{2+}$ . Previous work on  $L$ -shell photoionization of  $\text{Fe}^{2+}$  ions reported theoretical calculations of cross sections for direct photoionization of an  $L$ -shell electron (Reilman & Manson 1979; Verner et al. 1993) and theoretical calculations of the deexcitation cascades that evolve after the removal of a  $2s$  or a  $2p$  electron (Kaastra & Mewe 1993; Kučas et al. 2019, 2020).

## 2. Experiment

The experiment was performed at the end station PIPE (Schippers et al. 2014; Müller et al. 2017; Schippers et al. 2020) of the photon beamline P04 (Viefhaus et al. 2013) at the synchrotron light source PETRA III, which is operated by DESY in Hamburg, Germany. As for our previous work on  $L$ -shell photoionization of  $\text{Fe}^+$  and  $\text{Fe}^{3+}$  (Schippers et al. 2017;

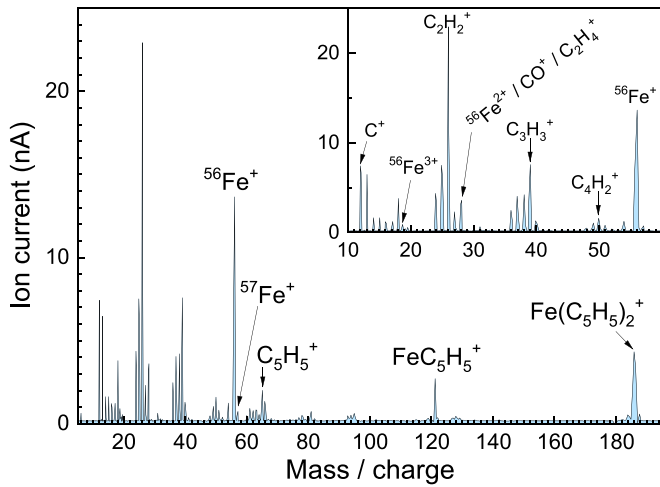


**Figure 1.** Measured primary-ion mass/charge spectrum. The inset enlarges the region of the spectrum that contains the  $\text{Fe}^+$ ,  $\text{Fe}^{2+}$ , and  $\text{Fe}^{3+}$  signals.

Beerwerth et al. 2019), we have employed the photon-ion merged-beams technique (for recent overviews, see Schippers et al. 2016b; Schippers & Müller 2020) to measure cross sections for single and multiple photoionization of  $\text{Fe}^{2+}$  ions. The experimental photon-energy range was 690–920 eV. The photon-energy bandwidth was about 1.0 eV corresponding to the FWHM of a Gaussian distribution function. The maximum energy-dependent photon flux was  $8 \times 10^{13} \text{ s}^{-1}$ . For an accurate determination of the photon energy scale, the same calibration was used as for the measurements with  $\text{Fe}^+$  (Schippers et al. 2017), taking into account the differences in the Doppler shift between the faster  $\text{Fe}^{2+}$  ions and the slower  $\text{Fe}^+$  ions. The remaining  $1\sigma$  uncertainty of the experimental photon-energy scale is  $\pm 0.2$  eV.

The  $\text{Fe}^{2+}$  ion beam was produced by leaking ferrocene,  $\text{Fe}(\text{C}_5\text{H}_5)_2$ , vapor into an electron-cyclotron resonance ion source (Schlapp et al. 1995) operated on an electrostatic potential of 6 kV. The extracted ion beam was mass/charge analyzed by passing it through a double-focusing dipole magnet. Figure 1 shows the composition of the ion beam as a function of mass-to-charge ratio with mass measured in atomic mass units and charge in the elementary charge unit. This mass/charge spectrum was obtained by scanning the magnetic field strength of the analyzing magnet and simultaneously recording the ion current collected in a Faraday cup. The  $^{56}\text{Fe}^{2+}$  signal occurs at a mass-to-charge ratio of 28. Other species, such as  $\text{CO}^+$  and  $\text{C}_2\text{H}_4^+$  are also expected to contribute to the measured ion current at this mass/charge ratio. Pure  $\text{Fe}^{2+}$  beams could be obtained for the isotope  $^{57}\text{Fe}$ , but only at a much reduced ion current due to the relatively low natural abundance of this isotope of only 2.1% (Meija et al. 2016). The  $^{56}\text{Fe}^{2+}$  (including contaminants) and  $^{57}\text{Fe}^{2+}$  ion currents were up to 27 nA and 0.12 nA, respectively.

As described previously for single and multiple ionization of  $\text{Fe}^+$  ions (Schippers et al. 2017), relative cross sections  $\sigma_m$  for  $m$ -fold ionization ( $m = 1$ –5) were measured individually for each product ion  $\text{Fe}^{q+}$  with charge state  $q = m + 2$ . To this end, the product ions were magnetically separated from the primary ion beam and directed onto a detector operated in the single-particle counting mode. This charge separation ensured that any photoionized products from the contaminants of the  $^{56}\text{Fe}^{2+}$  primary ion beam did not reach the product-ion detector. For most of the present measurements, the potentially

contaminated  $^{56}\text{Fe}^{2+}$  beam was used, as it delivered much higher photoionization signals than those obtained using a pure  $^{57}\text{Fe}^{2+}$  beam. Relative cross sections were measured with the isotope  $^{57}\text{Fe}$  at a few selected photon energies and the  $^{56}\text{Fe}^{2+}$  data were scaled to match the  $^{57}\text{Fe}^{2+}$  relative cross sections.

In principle, the PIPE setup permits photoionization cross sections to be placed on an absolute scale, as was achieved in our work on photoionization of  $\text{Fe}^+$  ions (Schippers et al. 2017). This requires measuring the spatial profiles of the ion beam and the photon beam, from which the geometrical beam overlap factor can be obtained. For  $\text{Fe}^{3+}$ , such measurements could not be carried out because of a technical problem that could not be solved within the allocated beamtime (Beerwerth et al. 2019). Since the  $\text{Fe}^{2+}$  and the  $\text{Fe}^{3+}$  data were taken during the same beamtime, absolute cross sections could not be measured for  $\text{Fe}^{2+}$  as well. Following the same approach as for the  $\text{Fe}^{3+}$  data, we multiplied the relative cross sections by a common factor such that the cross-section sum

$$\sigma_{\Sigma} = \sum_{m=1}^5 \sigma_m \quad (1)$$

matches the theoretical absorption cross section of Verner et al. (1993) at 690 eV (see below). The implicit assumption that  $\sigma_{\Sigma}$  in Equation (1) represents the  $\text{Fe}^{2+}$  absorption cross section is justified because all significant reaction channels were measured. This normalization procedure was motivated by the fact that the absolute experimental cross section for photo-absorption of  $\text{Fe}^+$  agrees with the corresponding theoretical cross section of Verner et al. (1993) within the  $\pm 15\%$  total experimental uncertainty at a 90% confidence level (Schippers et al. 2017).

### 3. Theory

For a deeper insight into the experimental findings, we performed theoretical calculations using the relativistic Multi-Configuration Dirac-Fock (MCDF) method (Grant 2007) and the Hartree-Fock method with relativistic extensions (HFR; Cowan 1981). The use of these methods has been described more extensively in our publications on photoionization of  $\text{Fe}^+$  and  $\text{Fe}^{3+}$  (Schippers et al. 2017; Beerwerth et al. 2019). Here, these methods were used to calculate  $\text{Fe}^{2+}$  absorption cross sections, accounting for direct ionization of a  $2p$  electron and for the excitation of a  $2p$  electron from the  $\text{Fe}^{2+}(1s^2 2s^2 2p^6 3s^2 3p^6 3d^6)$  ground configurations to higher  $nd$  and  $n's$  subshells. We included  $3 \leq n \leq 5$  and  $4 \leq n' \leq 5$  in the MCDF calculations. In the HFR calculations, we have only considered  $2p \rightarrow 3d$  excitations where the mixing of the configurations  $3d^n 4s^2$ ,  $3d^{n+1} 4s$ , and  $3d^{n+2}$  has been included in the initial, the excited and the final levels. Both the HFR and MCDF calculations account for direct single ionization of  $L$ -shell and  $M$ -shell electrons.

The MCDF computational tools allow for the modeling of the deexcitation pathways due to Auger cascade processes that accompany the initial creation of a  $2p$  hole. Since the focus of our investigations is on the resonance features that are associated with  $2p$  excitation, we did not consider cascades initiated by  $2s$ -hole creation. We used the GRASP2K (Jönsson et al. 2007) program package to generate the approximate wave functions and employed the tools of the RATIP code (Fritzsche 2001, 2012) to compute the required cross sections and transition rates. The same approach was used for  $\text{Fe}^{2+}$  as was used in our work on  $\text{Fe}^{3+}$  (Beerwerth et al. 2019), where more details are given. Briefly, the

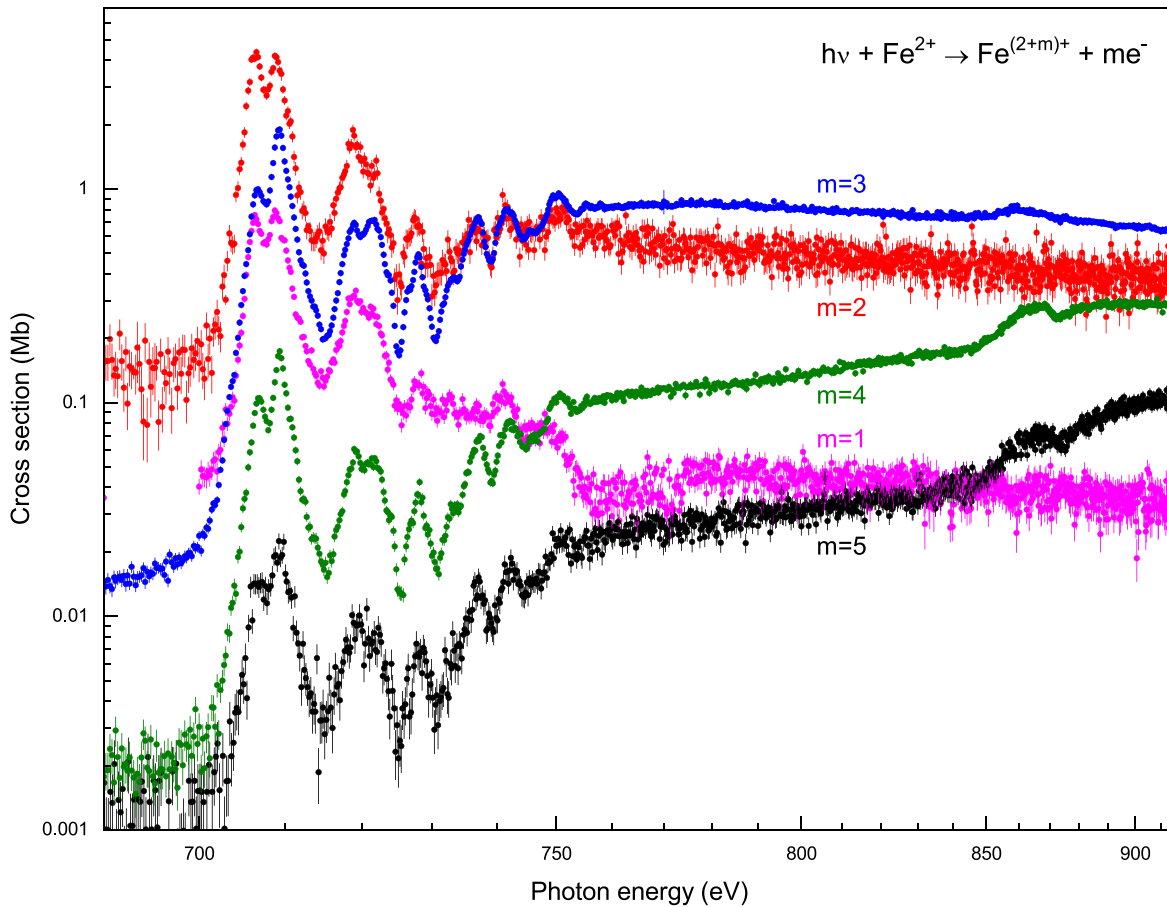


**Figure 2.** Measured partial cross sections  $\sigma_m$  for  $m$ -fold photoionization of  $\text{Fe}^{2+}$ . For a better view of the low-energy resonance structures, the energy scale is compressed toward high photon energies according to the formula  $E' = \sqrt{\log(E - 600 \text{ eV})}$ . The absolute cross-section scale ( $1 \text{ Mb} = 10^{-18} \text{ cm}^2$ ) was obtained by scaling the cross-section sum (Equation (1)) to the theoretical cross section for photoabsorption (see the text).

cascade includes all energetically allowed (two-electron) Auger processes where one of the electrons fills a lower subshell and another is ejected from the ion. In addition we accounted for three-electron Auger decays where a third electron undergoes a shake-down transition. The inclusion of these generally weak decay channels has been found to be essential to explain the highest product charge states obtained experimentally (Schippers et al. 2016b, 2017; Beerwerth et al. 2019). In order to keep the computations manageable, we assume that the radiative losses are negligible, i.e., that all levels that are energetically allowed to autoionize will do so. Cascades initiated by direct  $L$ -shell ionization of  $\text{Fe}^{2+}$  were previously calculated by Kaastra & Mewe (1993) and more recently by Kučas et al. (2019, 2020). In Section 4.1 below, we compare the results from these earlier studies with the present calculations.

#### 4. Results and Discussion

Our measured cross sections  $\sigma_m$  ( $1 \leq m \leq 5$ ) for single and multiple (up to five-fold) photoionization of  $\text{Fe}^{2+}$  ions are plotted in Figure 2 and also provided in Table 1 in numerical form. At photon energies of 690–750 eV, the dominant process is double ionization ( $m=2$ ). Up to  $\sim 749$  eV, a bound-bound transition forms a hole that can relax by emission of one or more electrons (with two being the dominant mode). Above  $\sim 749$  eV, a bound-free transition changes the charge state by one and forms a hole that can relax by emission of one or more electrons (with two being the dominant mode). In the theoretical cross sections of

Verner et al. (1993), this threshold for direct  $2p$  ionization occurs at 745.1 eV (Figure 3). The most obvious signature of this threshold in our data is the step-like decrease of the single-ionization cross section (magenta symbols in Figure 2) that sets in for energies  $\gtrsim 749$  eV. Below this threshold, a  $2p$  electron can only be resonantly excited to a higher partially occupied or unoccupied subshell, i.e., the primary photon-ion interaction does not change the charge state of the ion. At higher energies above the  $2p$  threshold, a  $2p$  electron can be directly ionized. This primary process increases the ion charge state by one. In both cases, a  $2p$  hole is created. The subsequent deexcitation of the multiply excited  $2p$ -hole configurations proceeds via a cascade of autoionization and radiative processes that produces the observed distributions over the various measured product charge states as already sketched in Section 3 and as will be discussed in more detail below.

The experimental absorption cross section (Equation (1)) is displayed in Figure 3, together with the theoretical absorption cross section of Verner et al. (1993). As explained above, the experimental cross-section scale was normalized to the theoretical one at a photon energy of about 690 eV. The theoretical cross section of Verner et al. (1993) does not contain any contribution from resonant photoionization. Thus, it clearly displays the calculated  $2p$  and  $2s$  thresholds at 745.1 and 863.1 eV, respectively. Comparatively weak signatures for the  $2s$  ionization threshold can also be seen in the experimental data in Figures 2 and 3. However, in the experimental cross

**Table 1**

Measured Cross Sections  $\sigma_m$  for  $m$ -fold Photoionization of  $\text{Fe}^{2+}$  ions (Figure 2), Resulting Sum Cross Section  $\sigma_\Sigma$  (Equation (1), Figure 3), and Mean Product Charge State  $\bar{q}$  (Equation (3), Figure 5(b))

Energy (eV)	$\sigma_1$ (Mb) <sup>a</sup>	$\sigma_2$ (Mb)	$\sigma_3$ (Mb)	$\sigma_4$ (Mb)	$\sigma_5$ (Mb)	$\sigma_\Sigma$ (Mb)	$\bar{q}$
691.062	0.0359(40)	0.155(30)	0.01454(11)	0.00178(36)	0.00203(59)	0.209(31)	3.94(73)
701.077	0.0404(33)	0.153(28)	0.0238(12)	0.00303(47)	0.00202(58)	0.222(28)	3.98(63)
710.091	0.771(15)	4.15(15)	1.7580(80)	0.1421(32)	0.0158(16)	6.84(16)	4.19(11)
720.107	0.315(10)	1.773(97)	0.6945(56)	0.0607(20)	0.0085(12)	2.852(97)	4.18(17)
750.153	0.0760(46)	0.801(66)	0.8789(66)	0.0959(25)	0.0214(18)	1.873(67)	4.56(18)
799.829	0.0416(47)	0.530(59)	0.820(20)	0.1291(28)	0.0325(27)	1.554(62)	4.73(21)
849.906	0.0376(47)	0.402(51)	0.735(18)	0.1936(34)	0.04688(33)	1.415(55)	4.87(20)
899.783	0.0344(47)	0.388(51)	0.6716(56)	0.2852(68)	0.0904(47)	1.469(52)	5.01(17)

**Notes.** The numbers in parentheses provide the  $1\sigma$  statistical experimental uncertainties. The systematic uncertainties of the photon-energy scale is  $\pm 0.2$  eV. The cross sections were put on an absolute scale by scaling  $\sigma_\Sigma$  to the theoretical absorption cross section of Verner et al. (1993) below 700 eV (see the text for details).

<sup>a</sup> 1 Mb =  $10^{-18}$  cm<sup>2</sup>.

(This table is available in its entirety in machine-readable form.)

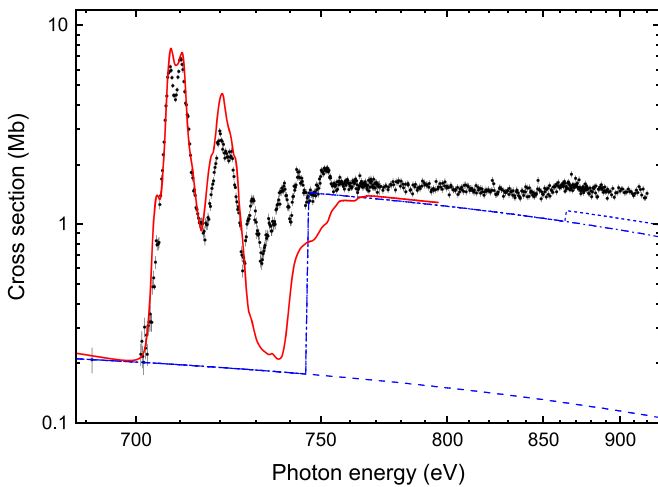


**Figure 3.** Experimental total absorption cross-section  $\sigma_\Sigma$  (Equation (1), symbols) and the theoretical subshell-resolved cross sections  $\sigma_m$  for photoionization by Verner et al. (1993, dashed line:  $\sigma_{3d} + \sigma_{3p} + \sigma_{3s}$ , dashed-dotted line:  $\sigma_{3d} + \sigma_{3p} + \sigma_{3s} + \sigma_{2p}$ , short-dashed line:  $\sigma_{3d} + \sigma_{3p} + \sigma_{3s} + \sigma_{2p} + \sigma_{2s}$ ) with the calculated thresholds for direct  $2p$  and  $2s$  ionization occurring at 745.1 and 863.1 eV, respectively. The corresponding results of our MCDF calculations (not shown) are practically identical to the results of Verner et al. (1993). The full line represents the result of the present HFR calculation assuming an initial statistical population of the various levels of the  $3d^6$  ground configuration and convoluted with a Gaussian of 1.0 eV FWHM. As in Figure 2, the energy scale is compressed for large energies to enhance the visibility of the low-energy resonance structures.

sections the thresholds are blurred by resonances associated with  $2p$  and  $2s$  excitation.

The dominant features in all measured cross sections are the two broad resonance structures at around 708 and 720 eV, which can be attributed to  $2p \rightarrow 3d$  excitations. The  $\sim 12$  eV energy difference between these two structures corresponds to the  $2p_{1/2,3/2}$  spin-orbit splitting. This splitting is reproduced by our present HFR calculations, which are also displayed in Figure 3. As already mentioned, the HFR calculations account for  $2p \rightarrow 3d$  excitations, but do not include the weaker resonances at higher energies, which are predominantly associated with  $2p \rightarrow nd$  excitations to higher subshells with  $n \geq 4$ . Hence, the HFR results lie below the measurements from  $\sim 730$ – $760$  eV. The HFR calculations also account for direct  $2p$  ionization, which is the dominant contribution to the  $\text{Fe}^{2+}$  absorption cross section at energies above 760 eV and continuing up to the highest experimental photon energy studied here.

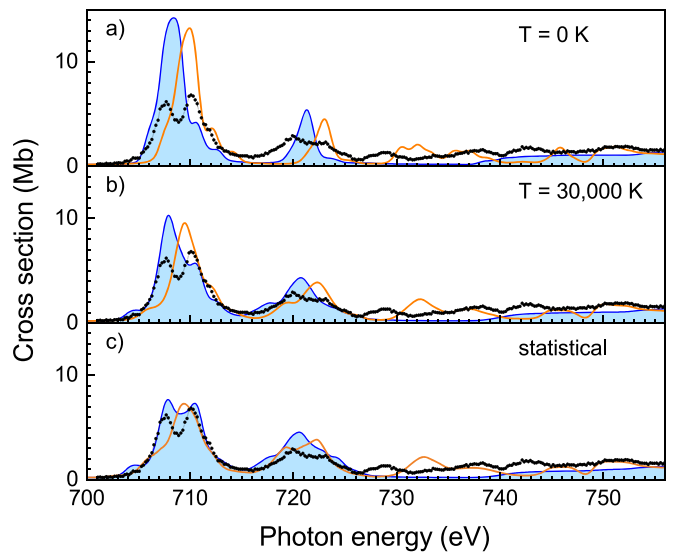


**Figure 4.** Computed absorption cross sections for different populations of the  $3d^6$  ground configuration compared with the experimental cross-section sum (full symbols) from Figure 3. The blue shaded and the orange full curves are the results of our HFR and MCDF calculations, which have been shifted by  $-2.5$  and  $-1.0$  eV, respectively, in order to align (by eye) the computed resonance structures with the experimental results. All theoretical cross sections were convoluted with a Gaussian with an FWHM of 1.0 eV in order to account for the experimental photon-energy bandwidth.

The  $\text{Fe}^{2+}([\text{Ar}] 3d^6)$  ground configuration splits into 34 fine-structure levels, which span an energy range of  $\sim 7$  eV (Kramida et al. 2019). It must be assumed that all excited levels were populated in the ion source. The lifetimes of these levels are sufficiently long that the excited ions partly survive the transport from the ion source to the photon-ion interaction region. Consequently, the ion beam consisted of a mixture of ions in different levels. Our MCDF and HFR calculations were carried out for all individual levels of the ground configuration. As shown in Figure 4, different assumptions on the initial level population in the ion beam lead to significantly different results for the calculated absorption cross sections. In Figure 4(a) we assumed a pure ground-level population. Figure 4(b) shows calculations for a Boltzmann distribution of energy levels for a temperature of 30,000 K. Figure 4(c) contains theoretical results for a statistical mixture of all levels pertaining to the  $\text{Fe}^{2+}$  ground configuration, where the population of each level is weighted by its degeneracy. Apparently, the latter provides

the best agreement with the experimental absorption cross section, if the theoretical resonance positions are uniformly shifted by  $-2.5$  and  $-1.0$  eV in case of the HFR and the MCDF calculations, respectively. Similar shifts were applied to the corresponding theoretical results for  $\text{Fe}^+$  and  $\text{Fe}^{3+}$  (Schippers et al. 2017; Beerwerth et al. 2019).

As already mentioned, the HFR calculations account for direct  $2p$  ionization and  $2p \rightarrow 3d$  excitation. Under the assumption of a statistical initial level distribution, the calculated cross section agrees rather well with the experimental absorption cross section in the energy range of the photoionization resonances that are associated with the  $2p \rightarrow 3d$  excitation. The resonances above  $\sim 726$  eV are related to the excitation of a  $2p$  electron to higher subshells such as the  $2p \rightarrow 4d$  and  $2p \rightarrow 5d$  excitations that were included in the MCDF calculations. But for the MCDF calculations, the agreement between the computed and experimental resonance structure is less satisfying, as compared to the HFR calculations (Figure 4). This is attributed to the rather limited consideration of configuration interaction by the present MCDF calculations, which were more geared toward the simulation of the deexcitation cascades that set in after the initial creation of the  $2p$  hole and that are discussed next.

#### 4.1. Cascade Calculations

From the measured cross sections  $\sigma_m$  for  $m$ -fold photoionization, the product charge-state fractions, i.e., the probabilities of an atom to end up in charge state  $q$ , can be derived as

$$f_q(E_{\text{ph}}) = \frac{\sigma_q}{\sigma_{\Sigma}}, \quad (2)$$

where  $\sigma_{\Sigma}$  is given by Equation (1). A key feature of the quantities  $f_q$  is that the systematic uncertainty of the absolute cross-section scale cancels out. The fractions  $f_q$  can also be used for the calculation of the mean product-charge state

$$\bar{q}(E_{\text{ph}}) = \sum_{q=3}^7 q f_q = \frac{1}{\sigma_{\Sigma}} \sum_{m=1}^5 (m+2) \sigma_m. \quad (3)$$

Figure 5 shows our experimental and theoretical product charge-state fractions following  $\text{Fe}^{2+}$  photoionization. Our MCDF calculations only account for cascades that follow the initial creation of a  $2p$ ,  $3s$ , or  $3p$  hole. Therefore, our theoretical values only apply to energies below the threshold for direct  $2s$  ionization at about 860 eV. The calculated product charge-state fractions follow the experimental values reasonably well considering the simplifications that were applied in order to keep the computations tractable. This is particularly true for the lower product charge states  $q = 3$  and 4. The theoretical values for  $q = 5$  agree with the corresponding experimental quantities only for energies above the threshold for direct  $2p$  ionization at about 750 eV. At lower energies the MCDF values for  $q = 5$  are much too small (they are essentially zero). The MCDF calculations significantly underestimate the production of the product charge state  $q = 6$  over the entire experimental energy range. The calculations do not predict any sizeable  $q = 7$  fraction. We attribute this increasing failure of our MCDF cascade model with increasing charge state to a mismatch of the computed (auto)ionization thresholds and to the neglect of many-body processes in the cascade calculations beyond the three-electron processes mentioned in Section 3. At present, such detailed calculations cannot be easily carried out for complex ions such as  $\text{Fe}^{2+}$  within our MCDF framework,

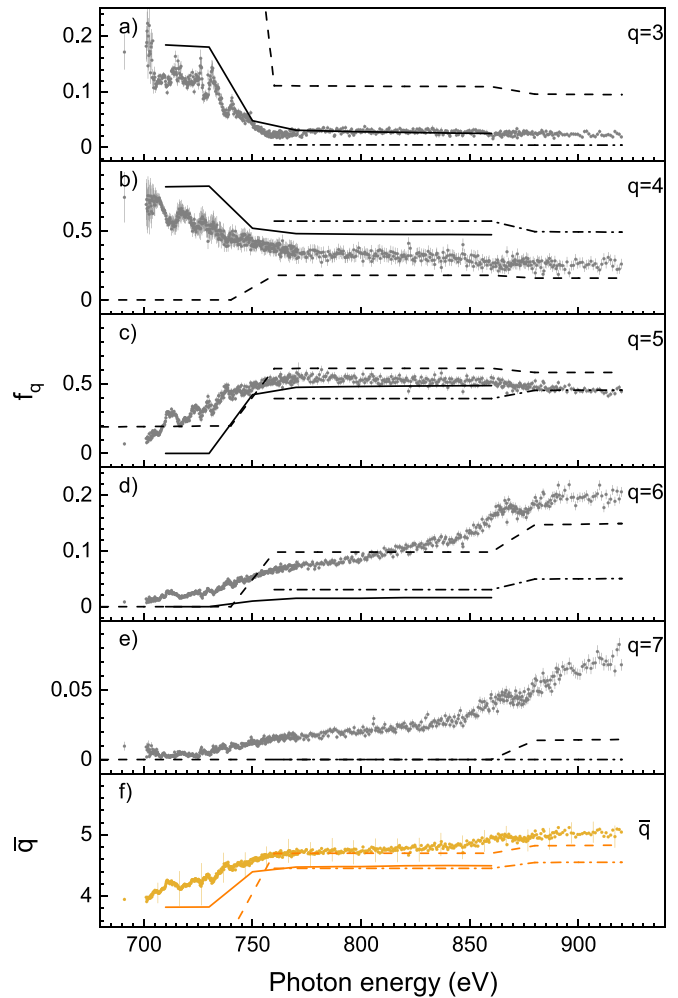


**Figure 5.** Product charge-state fractions  $f_q$  populated by photoionization of  $\text{Fe}^{2+}$  for panels (a)  $q = 3$ , (b)  $q = 4$ , (c)  $q = 5$ , (d)  $q = 6$ , and (e)  $q = 7$ : experimental results (gray symbols) are compared to our MCDF computations (full lines) and to the theoretical results by Kaastra & Mewe (1993, dashed lines) and by Kučas et al. (2019, 2020, dashed-dotted lines), both weighted by the subshell-specific photoionization cross sections of Verner et al. (1993) that are displayed in Figure 3. There is no full line in panel (e) since our MCDF cascade model does not predict any seven-fold charged product ions. Panel (f): mean charge state derived from the experimental data (orange symbols) and our cascade calculations (full line). The dashed lines and dashed-dotted lines result from the subshell specific charge fractions of Kaastra & Mewe (1993) and of Kučas et al. (2019, 2020), respectively, in combination with the subshell specific ionization cross sections of Verner et al. (1993).

although more advanced cascade computations, based on detailed cascade trees, are under way (Fritzsche 2019).

Earlier work on cascades, after inner-shell ionization of  $\text{Fe}^{2+}$ , has been carried out by Kaastra & Mewe (1993) and more recently by Kučas et al. (2019, 2020). These authors calculated the product charge-state distributions resulting from the removal of an inner-shell electron and the subsequent deexcitation cascades. In order to compare these results with the measured product charge-state fractions, the individual distributions for each inner-shell hole have to be weighted by the corresponding cross sections for inner-shell ionization (Schippers et al. 2017; Beerwerth et al. 2019). To this end, we used the subshell specific photoionization cross sections of Verner et al. (1993) that are displayed in Figure 3. The resulting product charge-state fractions are also displayed in Figure 5. The overall agreement of the results of Kaastra & Mewe (1993) with the experimental findings is not as good as compared

to our MCDF calculations, in particular for the lowest two product-ion charge states. For the higher product charge states the agreement is somewhat better. Kučas et al. (2019, 2020) have only considered the production of initial  $2p$  and  $2s$  holes. Therefore, their values can only be applied at energies above the  $2p$  ionization threshold and are biased toward higher product charge states. They significantly underestimate the production of  $\text{Fe}^{6+}$ . The Kučas et al. (2019, 2020) results for  $q = 4$  and  $5$  are in reasonable agreement with our MCDF and experimental results, given the various limitations of the theories. The agreement with the Kaastra & Mewe (1993) results is only reasonable for  $q = 5$ . Single ionization is severely underestimated by Kučas et al. (2019, 2020).

None of the above discussed cascade calculations reproduces the experimental findings for the product charge-state fractions  $f_q$  in all the details. This is likely due to the considerable complexity of the problem under consideration which, currently, can only be treated by making simplifying assumptions and by neglecting higher order processes such as direct double ionization, which probably form a wide continuum of cross-section contributions. Nevertheless, as shown in Figure 5, all methods agree reasonably well with the experimental findings (Table 1) for the photon-energy dependent mean charge state  $\bar{q}$  (Equation (3)).

#### 4.2. Summary of the Experimental and Theoretical Absorption Cross Sections for Neutral and Low-charged Iron

The present paper is the last in a sequence of publications on photoionization of low-charged iron ions. Therefore, we can now provide a comparison with our previous work on  $\text{Fe}^+$  (Schippers et al. 2017) and on  $\text{Fe}^{3+}$  (Beerwerth et al. 2019) with a focus on the most prominent features in the iron  $L$ -shell photoabsorption. In particular, these features should be useful for the identification of gas-phase iron in the ISM. Figure 6 displays our experimental and theoretical results for  $\text{Fe}^+$ ,  $\text{Fe}^{2+}$ , and  $\text{Fe}^{3+}$  ions and also the corresponding results for neutral iron atoms of Richter et al. (2004). In Figure 6, their  $\text{Fe}^0$  relative experimental cross sections were multiplied by an energy-independent factor to scale them to the theoretical cross-section scale. All the theoretical cross sections that are displayed in this figure are HFR results (see Section 3) for statistical mixtures of ground-configuration levels as discussed in Section 4 for  $\text{Fe}^{2+}$ . As already mentioned, the theoretical energy scales were shifted by eye in order to best line up the theoretical resonance positions with the experimental ones. The remaining minor discrepancies between theory and experiment are most likely due to the inherent limitations of the theoretical method and uncertainties in the level populations for the experimental results. In the following we thus use the experimentally benchmarked theoretical cross sections for the comparison with absorption cross sections for solid materials that are expected to be present in interstellar dust particles.

### 5. Comparison with Other Forms of Iron

The nature of the chemical binding of iron to interstellar dust particles is currently being debated. For example, from experiments in microgravity, Kimura et al. (2017) concluded that the probability of the formation of pure iron grains should be very low and that, consequently, iron should be bound in iron compounds or accreted as impurities on other grains in the ISM. Another hypothesis was pursued by Bilalbegović et al. (2016) who

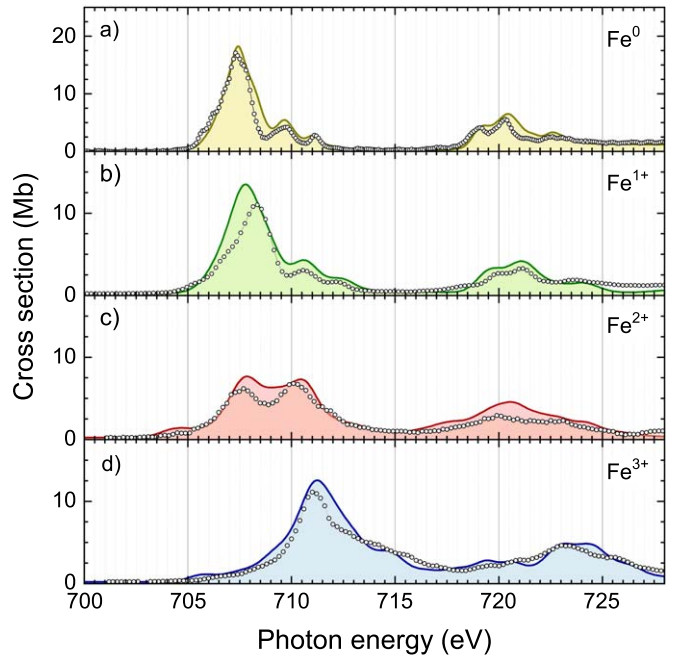


**Figure 6.** Experimental (symbols) and HFR (full shaded curves) photoabsorption cross sections of (a)  $\text{Fe}^0$ , (b)  $\text{Fe}^+$ , (c)  $\text{Fe}^{2+}$ , and (d)  $\text{Fe}^{3+}$ . The  $\text{Fe}^0$ ,  $\text{Fe}^+$ , and  $\text{Fe}^{3+}$  data have been taken from Richter et al. (2004), Schippers et al. (2017), and Beerwerth et al. (2019), respectively. The theoretical cross sections are for statistical mixtures of ground-configuration levels and account for the experimental photon-energy bandwidth, which was  $\sim 0.6$  eV for  $\text{Fe}^0$  and  $\sim 1$  eV for  $\text{Fe}^+$ ,  $\text{Fe}^{2+}$ , and  $\text{Fe}^{3+}$ . The  $1\sigma$  uncertainty of the experimental photon-energy scale is  $\pm 0.2$  eV for  $\text{Fe}^+$ ,  $\text{Fe}^{2+}$ , and  $\text{Fe}^{3+}$  and unspecified for  $\text{Fe}^0$ .

calculated infrared absorption spectra of hydrogenated iron particles. From a variety of astronomical observations and related astrophysical modeling, several groups inferred that a large fraction of the iron in the ISM could be incorporated as inclusions in silicate grains (Zhukovska et al. 2018; Westphal et al. 2019; Zafar et al. 2019). Using an ion implantation technique, Leveueur et al. (2011) produced Fe nanoparticles in silica, which could serve as a proxy for iron locked in interstellar dust particles. In addition, Lee et al. (2009) have carefully measured absorption data for a number of iron compounds.

Figure 7 presents a comparison of the experimentally benchmarked theoretical gas-phase data for neutral and low-charged ions with the absorption cross sections for solid iron and solid iron compounds of Lee et al. (2009) and Leveueur et al. (2011). The theoretical gas-phase data are different from those displayed in Figure 6 where statistical populations of several levels were considered in order to account for the high temperatures in the ion source. The temperatures in the ISM are considerably lower such that usually only the ground levels are significantly populated. This is accounted for in the theoretical data for  $\text{Fe}^0$ ,  $\text{Fe}^+$ ,  $\text{Fe}^{2+}$ , and  $\text{Fe}^{3+}$  displayed in Figure 7. In addition, a finite photon energy bandpass was considered by convoluting the theoretical cross sections with Gaussians with FWHM of 1.0 eV and 0.24 eV. The latter energy spread corresponds to a resolving power  $E/\Delta E = 3000$  as was used in the experiments of Lee et al. (2009). This resolving power approximately corresponds to what is currently foreseen for the future Athena X-ray telescope (Barret et al. 2020).

When comparing X-ray absorption data from different sources, the calibration uncertainties of the different photon energy scales are an issue of concern. For the  $\text{Fe}^+$ ,  $\text{Fe}^{2+}$ , and

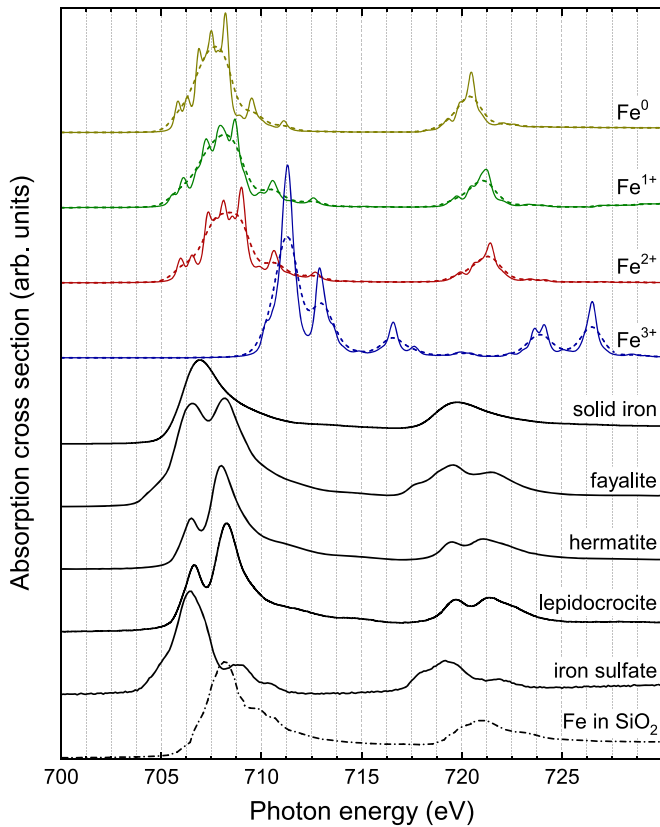


**Figure 7.** Comparison of photoabsorption cross sections for gas-phase neutral and low-charged ions with photoabsorption cross sections for solid iron and solid iron-bearing compounds. The cross sections for  $\text{Fe}^0$ ,  $\text{Fe}^{1+}$ ,  $\text{Fe}^{2+}$ , and  $\text{Fe}^{3+}$  (colored lines) are the experimentally benchmarked HFR results for photoabsorption of the ground level only. The full and the dashed colored lines were calculated taking into account photon energy spreads of 0.24 eV and 1.0 eV, respectively. The data for solid iron and iron-bearing compounds have been taken from the work of Lee et al. (2009, black full lines) and (Leveneur et al. 2011, black dashed-dotted line). The  $1\sigma$  uncertainty of the experimental photon-energy scale is  $\pm 0.2$  eV for  $\text{Fe}^{1+}$ ,  $\text{Fe}^{2+}$ , and  $\text{Fe}^{3+}$ ,  $\pm 0.4$  eV for Fe in  $\text{SiO}_2$  (J. Leveneur 2020, private communication) and unspecified for the other samples (see the text).

$\text{Fe}^{3+}$  absorption cross sections this uncertainty is  $\pm 0.2$  eV. For Fe in  $\text{SiO}_2$  it is  $\pm 0.4$  eV (J. Leveneur 2020, private communication). Richter et al. (2004) do not provide any information on the calibration uncertainty of the  $\text{Fe}^0$  energy scale. In our experiments, absorption features in gases were used as reference standards as discussed in considerable detail by Müller et al. (2017, 2018). Lee et al. (2009) refer their data to theoretically calculated values for the iron  $2p$  absorption edges as provided by the computer code of Brennan & Cowan (1992), which uses theoretical absorption data from Cromer & Liberman (1970, 1981). This calibration is problematic for two reasons. First, the experimental data do not exhibit a clear step-like threshold absorption feature since this is masked by the near-threshold photoabsorption resonances. Second, the uncertainties of the theoretical calculations are unknown and may be rather large. For example, in their comprehensive list of X-ray calibration features, Deslattes et al. (2003) quote a difference between theoretical and experimental values for the iron  $L_3$  edge of 2 eV. This value is in line with the  $-2.2$  eV energy shift that we applied in benchmarking the present theoretical HFR results for photoabsorption of  $\text{Fe}^{2+}$ . This uncertainty of the solid-state data hampers a quantitative comparison between gas-phase and solid-state absorption data.

In any case, the differences will become more apparent at higher spectral resolving powers such as those envisaged for future X-ray telescopes.

## 6. Summary and Conclusions

This publication concludes a sequence of papers (Schippers et al. 2017; Beerwerth et al. 2019) on the photoionization of low-charged  $\text{Fe}^{q+}$  ions with  $q = 1, 2$ , and 3 that was designed to provide accurate data for resonant  $L$ -shell photoabsorption in order to enable the identification of these ion species in the ISM medium and their discrimination against solid-phase iron locked up in dust grains. The experimental cross sections for  $m$ -fold ionization ( $m = 1-5$ ) for  $\text{Fe}^{2+}$  were obtained by using the photon-ion merged-beams technique at a synchrotron light source. The cross-section data exhibit strong absorption features associated with the excitation of a  $2p$  electron to higher atomic subshells. The positions and relative peak intensities of these features can serve as clear fingerprints for the various iron charge states investigated. We have also carried out quantum theoretical calculations of photoabsorption by  $\text{Fe}^{2+}$  ions. Furthermore, we have calculated the deexcitation cascades that follow the creation of a  $2p$  hole and that determine the final charge state distributions.

Using our combined experimental and theoretical results, we can generate the photoabsorption data needed to model X-ray observations of the ISM. The experimental results are particularly important for providing experimental benchmarks for the theoretical energy scale. Because of the many-body nature of the problem, the calculated energies of the  $L$ -shell absorption features have rather large uncertainties. Thus, our experimental benchmarking is vital for achieving the level of accuracy required for astronomical observations. The energy-shifted theoretical results can then be used to generate the needed photoabsorption cross-section data for cold ions, similar to those expected in the ISM. The experimental results cannot be directly used due to the initial level distribution of the ions corresponding to a much higher temperature than the cold ISM. A direct comparison of the present gas-phase absorption cross section with absorption data for iron-bearing condensed matter compounds from the literature is also hampered by the unknown uncertainties of the photon-energies in these studies. Future work on solid-state absorption data is needed to address this issue.













Our calculations of the Auger cascades that evolve after the primary creation of a  $2p$  hole by excitation or direct ionization yield charge-state fractions that are in reasonable agreement with the experimental findings for the lowest two product-ion charge states,  $\text{Fe}^{3+}$  and  $\text{Fe}^{4+}$ . This is a clear improvement as compared to earlier work by Kaastra & Mewe (1993) and by Kučas et al. (2019, 2020). The higher product-ion charge states are not as well described. This is attributed to the simplifications that had to be made in order to keep the computations tractable. For example, our calculations neglected double shake processes that were found to be important for an accurate description of cascades in a lighter ion (Schippers et al. 2016a). A further development of the atomic structure codes—such as currently pursued by Fritzsche (2019)—is required to properly account for the many-electron contributions and a sufficiently large set of decay paths also for heavier ions.

We thank Lía Corrales, Eric Gotthelf, Julia Lee, Tim Kallman, and Frits Paerels for stimulating discussions. We

acknowledge DESY (Hamburg, Germany), a member of the Helmholtz Association HGF, for the provision of experimental facilities. Parts of this research were carried out at PETRA III and we would like to thank Gregor Hartmann, Frank Scholz, and Jörn Seltmann for assistance in using beamline P04.

This research has been funded in part by the German Federal Ministry for Education and Research (BMBF) within the “Verbundforschung” funding scheme under contracts 05K16GUC, 05K16RG1, and 05K16SJA. S.B. and K.S. acknowledge funding from the Initiative and Networking Fund of the Helmholtz Association through the Young Investigators Group program and the SFB 755, “Nanoscale photonic imaging, project B03.” D.W.S. was supported, in part, by the NASA Astrophysics Research and Analysis Program and the Astrophysics Data Analysis Program. The participation of RAP in the experiment was supported by funds from the Alexander von Humboldt Foundation.

### ORCID iDs

Stefan Schippers  <https://orcid.org/0000-0002-6166-7138>  
 Randolph Beerwerth  <https://orcid.org/0000-0001-5100-4229>  
 Sadia Bari  <https://orcid.org/0000-0003-3985-2051>  
 Ticia Buhr  <https://orcid.org/0000-0003-3337-1740>  
 Kristof Holste  <https://orcid.org/0000-0001-8809-1696>  
 A. L. David Kilcoyne  <https://orcid.org/0000-0002-8805-8690>  
 Alexander Perry-Sassmannshausen  <https://orcid.org/0000-0002-0700-3875>  
 Daniel Wolf Savin  <https://orcid.org/0000-0002-1111-6610>  
 Kaja Schubert  <https://orcid.org/0000-0002-6362-4262>  
 Stephan Fritzsche  <https://orcid.org/0000-0003-3101-2824>  
 Michael Martins  <https://orcid.org/0000-0002-1228-5029>  
 Alfred Müller  <https://orcid.org/0000-0002-0030-6929>

### References

- Barret, D., Decourchelle, A., Fabian, A., et al. 2020, *AN*, **341**, 224  
 Beerwerth, R., Buhr, T., Perry-Sassmannshausen, A., et al. 2019, *ApJ*, **887**, 189  
 Bilalbegović, G., Maksimović, A., & Mošaček-Grošev, V. 2016, *MNRAS*, **466**, L14  
 Blancard, C., Cubaynes, D., Guilbaud, S., & Bizau, J.-M. 2018, *ApJ*, **853**, 32  
 Brennan, S., & Cowan, P. L. 1992, *RSci*, **63**, 850  
 Cowan, R. D. 1981, *The Theory of Atomic Structure and Spectra* (Berkeley, CA: California Univ. Press)  
 Cromer, D. T., & Liberman, D. 1970, *JChPh*, **53**, 1891  
 Cromer, D. T., & Liberman, D. A. 1981, *AcCrA*, **37**, 267  
 Deslattes, R. D., Kessler, E. G., Indelicato, J. P., et al. 2003, *RvMP*, **75**, 35  
 Fritzsche, S. 2001, *JESRP*, **114**, 1155  
 Fritzsche, S. 2012, *CoPhC*, **183**, 1525  
 Fritzsche, S. 2019, *CoPhC*, **240**, 1  
 Grant, I. P. 2007, *Relativistic Quantum Theory of Atoms and Molecules: Theory and Computation* (New York: Springer)  
 Jönsson, P., He, X., Froese-Fischer, C., & Grant, I. P. 2007, *CoPhC*, **177**, 597  
 Kaastra, J. S., & Mewe, R. 1993, *A&AS*, **97**, 443  
 Kimura, Y., Tanaka, K. K., Nozawa, T., Takeuchi, S., & Inatomi, Y. 2017, *SciA*, **3**, e1601992  
 Kortright, J. B., & Kim, S.-K. 2000, *PhRvB*, **62**, 12216  
 Kramida, A., Ralchenko, Y., Reader, J., & Team, N. A. 2019, *NIST Atomic Spectra Database* (version 5.7.1) (Gaithersburg, MD: National Institute of Standards and Technology), <http://physics.nist.gov/asd>  
 Kučas, S., Drabužinskis, P., & Jonauskas, V. 2020, *ADNDT*, **135**, 101357  
 Kučas, S., Drabužinskis, P., Kynienė, A., Masys, Š., & Jonauskas, V. 2019, *JPhB*, **52**, 225001  
 Lee, J. C., Xiang, J., Ravel, B., Kortright, J., & Flanagan, K. 2009, *ApJ*, **702**, 970  
 Leveneur, J., Waterhouse, G. I. N., Kennedy, J., Metson, J. B., & Mitchell, D. R. G. 2011, *JPC*, **115**, 20978  
 Meija, J., Tyler, C. B., Berglund, M., et al. 2016, *PAPCh*, **88**, 293  
 Miedema, P. S., & de Groot, F. M. F. 2013, *JESRP*, **187**, 32  
 Müller, A., Bernhardt, D., Borovik, A., Jr., et al. 2017, *ApJ*, **836**, 166  
 Müller, A., Lindroth, E., Bari, S., et al. 2018, *PhRvA*, **98**, 033416  
 Reilman, R. F., & Manson, S. T. 1979, *ApJS*, **40**, 815  
 Richter, T., Godehusen, K., Martins, M., Wolff, T., & Zimmermann, P. 2004, *PhRvL*, **93**, 023002  
 Schippers, S., Beerwerth, R., Abrok, L., et al. 2016a, *PhRvA*, **94**, 041401  
 Schippers, S., Buhr, T., Borovik, A., Jr., et al. 2020, *XRS*, **49**, 11  
 Schippers, S., Kilcoyne, A. L. D., Phaneuf, R. A., & Müller, A. 2016b, *ConPh*, **57**, 215  
 Schippers, S., Martins, M., Beerwerth, R., et al. 2017, *ApJ*, **849**, 5  
 Schippers, S., & Müller, A. 2020, *Atoms*, **8**, 45  
 Schippers, S., Ricz, S., Buhr, T., et al. 2014, *JPhB*, **47**, 115602  
 Schlapp, A., Trassl, R., Salzborn, E., et al. 1995, *NIMPB*, **98**, 525  
 Simon, M. C., Crespo López-Urrutia, J. R., Beilmann, C., et al. 2010, *PhRvL*, **105**, 183001  
 Verner, D. A., Yakovlev, D. G., Band, I. M., & Trzhaskovskaya, M. B. 1993, *ADNDT*, **55**, 233  
 Viehhaus, J., Scholz, F., Deinert, S., et al. 2013, *NIMPA*, **710**, 151  
 Westphal, A. J., Butterworth, A. L., Tomsick, J. A., & Gainsforth, Z. 2019, *ApJ*, **872**, 66  
 Zafar, T., Heintz, K. E., Karakas, A., Lattanzio, J., & Ahmad, A. 2019, *MNRAS*, **490**, 2599  
 Zhukovska, S., Henning, T., & Dobbs, C. 2018, *ApJ*, **857**, 94